Ultrathin Pt and Mo films on $Al_{1-x}Sc_xN$: an Interface Investigation

Yishui Ding[a,b], Xiangyu Hou[b,*], Tengyu Jin[a,c,*], Yanan Wang[c], Xu Lian[b], Yuan Liu[a,b], Yihe Wang[a,b], Sisheng Duan[c], Xiangrui Geng[b], Meng Wang[a,b], Jingyu Mao[c], Yuanyuan Zhang[c], Peirong Tang[b], Minghua Li[d], Huamao Lin[d], Yao Zhu[d], Siewlang Teo[e], Qiang Zhu[e], Ming Lin[e,*], Wei Chen[a, b, c, f,*]

a Joint School of National University of Singapore and Tianjin University, International Campus of Tianjin University, Binhai New City, Fuzhou 350207, PR China
b Department of Chemistry, National University of Singapore, 3 Science Drive 3, 117543, Singapore
c Department of Physics, National University of Singapore, 2 Science Drive 3, 117542, Singapore
d Institute of Microelectronics, Agency for Science, Technology and Research (A*STAR), 2 Fusionopolis Way, Singapore 138634, Singapore
e Institute of Materials Research and Engineering (IMRE), Agency for Science, Technology and Research (A*STAR), 2 Fusionopolis Way, Singapore 138634, Singapore
f National University of Singapore (Suzhou) Research Institute, 377 Lin Quan Street, Suzhou 215123, PR China
* Corresponding Author E-mail: houxy@nus.edu.sg (Xiangyu HOU), tengyujin@u.nus.edu (Tengyu JIN), m-lin@imre.a-star.edu.sg (Ming LIN) and phycw@nus.edu.sg (Wei CHEN)

Abstract

Aluminum scandium nitride ($Al_{1-x}Sc_xN$) with attractive ferroelectric and piezoelectric properties is a promising material for next-generation device applications. However, the understanding of interface properties between integrated ultrathin metal electrodes and $Al_{1-x}Sc_xN$ films is still limited, despite their significant impact on device performance. In the study, we investigated the growth mechanism and interfacial chemistry of ultrathin platinum (Pt) and molybdenum (Mo) films deposited on the high-crystalline $Al_{1-x}Sc_xN$ (x = 0.2) surface. The chemical and electronic structure evolutions of the interface during the deposition process were probed by *in-situ* X-ray photoelectron spectroscopy (XPS) and ultraviolet photoelectron spectroscopy (UPS). The structural properties of the interface were further characterized by cross-sectional transmission electron microscopy (TEM), X-ray diffraction spectroscopy (XRD), and atomic force microscopy (AFM). Our results reveal the formation of ionic Pt^{2+}-N bonds at the Pt/$Al_{1-x}Sc_xN$ interface, while Mo does not bond with the substrate. Furthermore, we identified electron transfer induces upward band-bending like effects on the $Al_{1-x}Sc_xN$ surface upon both Pt and Mo interactions. Our work on the chemical and structural research of ultrathin metal electrodes and $Al_{1-x}Sc_xN$ interfaces provides guidance towards designing high-performance micro-electromechanical (MEMS) devices.

Keywords: $Al_{1-x}Sc_xN$, Pt, Mo, *in-situ* XPS/UPS, cross-sectional TEM

1 Introduction

With the gradually crowed mobile spectrum and emerging development of the 5G applications, high-performance acoustic filters possessing wide bandwidth and low insertion loss are urgently needed for wireless communication, especially the mm-wave applications. Besides conventional piezoelectric materials such as langasite or langatate have been used in the telecommunication industry [1, 2], aluminum nitride (AlN) with its wurtzite structure in the III-V (nitride) group, presents a promising alternative [3-5]. AlN exhibits a high acoustic velocity (~5700 m/s), decent thermal conductivity and stability, as well as its compatibility with complementary metal-oxide-semiconductor (CMOS) technology [6-8]. By doping AlN with scandium (Sc), the formed $Al_{1-x}Sc_xN$ material exhibits enhanced piezoelectric and electromechanical performance while maintaining CMOS compatibility [9-11]. For example, recent research has demonstrated that $Al_{1-x}Sc_xN$ with x approaching 43% exhibits a 400% increase in the piezoelectric constant, while $Al_{1-x}Sc_xN$ films with a high Sc concentration (x > 0.27) demonstrate field-driven ferroelectric switching behavior [12, 13]. Additionally, the tunable polarization properties allows precise control over the resonance frequency and bandwidth of the resonators, enhancing their frequency selectivity and enabling their integration into diverse applications requiring high-performance acoustic filtering [14-17].

The trend of downscaled acoustic devices requires ultrathin metal electrodes to maintain a good contact with piezoelectric films. However, the concurrent electric resistivity increases dramatically when the metal thickness is scaled down to the nanoscale range (<100 nm). This thickness-dependent effect, called the finite size effect, is mainly due to the enhanced electron scattering at the interface in the nanoscale dimension, including the boundary of the metal or the metal/piezoelectric interface [18, 19]. Improving the quality of metal films with well-ordered atomic structures and constructing a smooth interface between metal and piezoelectric films are significant to suppress the scattering effect and control the metal resistivity at the reduced thickness. The realization of high-performance thin film $Al_{1-x}Sc_xN$-based micro-electromechanical (MEMS) devices depends on the ohmic and viscous losses of the chosen electrode material. Platinum (Pt) and molybdenum (Mo) electrodes are widely used as metal

electrodes integrated with $Al_{1-x}Sc_xN$ films due to their excellent electrical conductivity and good adhesion properties [20-22]. A lot of efforts have been focused on direct growth of AlN or $Al_{1-x}Sc_xN$ thin films on metallic bottom electrodes (Pt, Mo) to ensure high crystallinity, low defects, and residual stress. For example, Das et al. [23] reported the high quality AlN films grown on the bottom Mo electrode with a preferred (100) crystalline orientation, which exhibited excellent piezoelectric and mechanical properties. In addition, highly *c*-axis oriented $Al_{1-x}Sc_xN$ thin films with patterned Pt electrodes have displayed ferroelectric switching [24]. A recent study has also investigated the significant effect of the selected electrode material on the ferroelectricity of $Al_{1-x}Sc_xN$ films, including the difference in crystal orientation of the films grown on different metals and the inherent contact interfaces between the metal and the dielectric materials [25]. However, the behavior of the interface between the ultrathin electrodes (<30 nm) with low resistivity and $Al_{1-x}Sc_xN$ film remains elusive. Therefore, it is necessary to conduct in-depth studies of the metal deposition process and comprehend the metal deposition mechanism, i.e., the electronic and chemical structures of the metal and metal/$Al_{1-x}Sc_xN$ interface.

In this work, we use $Al_{1-x}Sc_xN$ ($x = 0.2$) to unravel the growth behavior and interfacial properties of ultrathin Pt and Mo films. *In-situ* x-ray photoelectron spectroscopy (XPS) and ultraviolet photoelectron spectroscopy (UPS) were employed to investigate the detailed electronic structures and chemical interactions of the interface. The structural properties and surface morphology of the $Al_{1-x}Sc_xN$, Pt/$Al_{1-x}Sc_xN$ and Mo/$Al_{1-x}Sc_xN$ heterostructures were further corroborated by cross-sectional transmission electron microscopy (TEM), X-ray diffraction (XRD) and atomic force microscopy (AFM). Our *in-situ* spectroscopy studies reveal that Pt replaces Al atoms in the wurtzite crystal structure by reacting with nitrogen, resulting in Pt^{2+}-N at the region near the Pt/$Al_{1-x}Sc_xN$ interface, while Mo does not react with the substrate. In particular, the evolution of the growth mechanism upon increasing metal thickness has been correlated with the structural and morphological changes of the contact surface and the metal/$Al_{1-x}Sc_xN$ interface. Our study provides valuable insights into the metal electrode deposition mechanism in $Al_{1-x}Sc_xN$ films.

2 Materials and methods

The 20 nm thick $Al_{0.8}Sc_{0.2}N$ thin film was prepared using a cluster Physical Vapor Deposition (PVD) system with pulsed DC reactive magnetron sputtering [26]. The sputtering chamber was equipped with a $Al_{0.8}Sc_{0.2}$ alloy target, while a 200 mm Si (100) wafer served as the substrate. Before the deposition of the film, high-temperature degas and wafer surface cleaning were performed. Reactive sputtering was carried out using Ar as the discharge gas and N_2 as the reactive gas. No additional substrate heating was used in the film deposition. Subsequently, $Al_{0.8}Sc_{0.2}N$ samples were transferred to an ultrahigh-vacuum (UHV) system, consisting of a sample load-lock chamber, a homemade preparation chamber, and a custom-designed UHV analysis chamber [27, 28]. The base pressures of both preparation and analysis chambers were maintained below 9×10^{-10} mbar.

In the preparation chamber, the $Al_{0.8}Sc_{0.2}N$ surface was initially cleaned using Ar^+ sputtering for several cycles until the XPS spectra of C 1s and O 1s regions in Fig. S1 with exhibited negligible oxygen and carbon contaminants. To study the growth behavior of the metal electrodes deposited on $Al_{0.8}Sc_{0.2}N$, platinum (Pt) or molybdenum (Mo) was evaporated onto the clean $Al_{0.8}Sc_{0.2}N$ film, followed by *in-situ* XPS/UPS measurements without breaking the vacuum. The Pt and Mo were vapor-deposited onto the clean $Al_{0.8}Sc_{0.2}N$ surface using e-beam heating of a Pt (99.9%, MaTeck) and Mo (99.95%, MaTeck) rod, respectively. The nominal thickness of the metal deposition was accurately calibrated using a quartz crystal microbalance (QCM, INFICON). Different metal thicknesses were achieved by varying the deposition time while maintaining the same deposition rate.

The analysis chamber was equipped with a SPECS XR-50 X-ray source that had Mg/Al twin anodes, a SPECS UVS 10/35 He I excitation source ($h\nu$ = 21.2 eV), and a SPECS Phoibos hemispherical energy analyzer for XPS/UPS measurements. The XPS core-level spectra were obtained using Al $K\alpha$ radiation ($h\nu$ = 1486.61 eV) at a take-off angle of 55 °. The UPS spectra of the valence region were collected with a -7 V bias voltage on the sample, and the take-off angle was fixed at 45°. The XPS spectra fitting was performed by CasaXPS, with Shirley-type

background subtracting. The GL(30) line shape was used to fit symmetric peaks, while the asymmetric peaks of metallic Pt and Mo were fit using the LA (1.2,85,70) and LA (1.2,2.3,2) line shape, respectively. Tables S1 and S2 in the Supplementary material provide peak fitting parameters such as peak positions, FWHM and peak area percentage.

The data obtained from various characterization techniques were analyzed to gain insights into the interfacial, structural, and morphological properties of the $Al_{0.8}Sc_{0.2}N$ films deposited with ultrathin Pt or Mo films. The $Al_{0.8}Sc_{0.2}N$ films were analyzed before and after depositing the Pt or Mo films to examine the effects of Pt or Mo interaction on the interface. Cross-section samples were prepared using a dual-beam focused ion beam (FIB) system (FEI Helios Nanolab 450S). TEM characterization and image acquisition were performed using an FEI Titan 80-300 TEM system operating at a 200 kV accelerating voltage. High-angle annular dark-field scanning transmission electron microscopy (HAADF-STEM) and Energy-dispersive X-ray spectroscopy (EDS) analyses were performed on a Tecnai 20F, equipped with an Oxford EDS detector and a Gatan Imaging Filter (GIF). Quantification results presented in TEM were calculated with Digital Micrograph software (DM, Gatan Inc., USA). The crystal orientations of the $Al_{0.8}Sc_{0.2}N$ thin films were characterized by a Bruker D8 Advance XRD. AFM characterization was performed using a Bruker Fastscan AFM.

3 Results and discussion

The morphology and structure of the 20 nm aluminium scandium nitride ($Al_{0.8}Sc_{0.2}N$) film grown on a Si(100) substrate were characterized in detail using high-resolution TEM, AFM and XRD. As shown in Fig. 1(a), the $Al_{0.8}Sc_{0.2}N$ film exhibits a successive columnar structure with geometrically necessary dislocations at the grain boundaries, likely due to varying in-plane orientation of the film. An average interplanar distance ($d_{spacing}$) of 0.25 nm can be observed, corresponding to the (0002) lattice plane spacing of the wurtzite crystalline phase in the $Al_{0.8}Sc_{0.2}N$ film. This shows the growth of highly oriented textures of $Al_{0.8}Sc_{0.2}$ on Si substrate, with (0002) planes parallel to Si(100) substrate. Instead of sharp diffraction spots, the inserted FFT image of $Al_{0.8}Sc_{0.2}N$ presents an arc shape for 0002 spots, indicating a slight tilting of

adjacent crystal columns to each other [29]. Fig. 1(b) presents the AFM image of the as-grown $Al_{0.8}Sc_{0.2}N$ film, indicating a low root-mean-square (RMS) surface roughness of 0.881 nm. The XRD analysis in Fig. 1(c) confirms the $Al_{0.8}Sc_{0.2}N$ crystalline structure, as the diffraction peaks at 36.02° correspond to the (0002) orientation of the crystal structure [30]. The absence of other peaks near the $Al_{0.8}Sc_{0.2}N$(0002) peak indicates a highly *c*-axis orientation [25, 31]. The rocking curve of the relatively thinner 20 nm $Al_{0.8}Sc_{0.2}N$ film shows a full width half maximum (FWHM) value of 0.58°, suggesting good crystallinity of the as-grown $Al_{0.8}Sc_{0.2}N$ film. These results confirm the high-quality growth of $Al_{0.8}Sc_{0.2}N$ film, which can be further used to explore the interfacial chemistry between the top metal electrodes and $Al_{1-x}Sc_xN$.

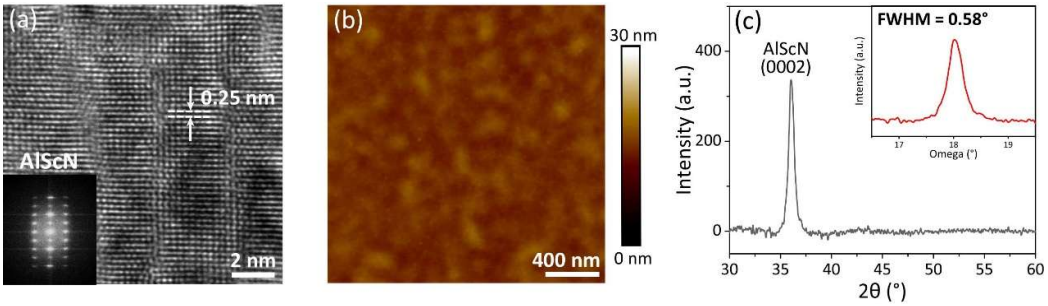

Fig. 1. Structural characterization of $Al_{0.8}Sc_{0.2}N$ film. (a) High-resolution TEM image. Inset: Fast Fourier Transform (FFT) diffraction pattern. (b) AFM image of the surface morphology. (c) XRD 2θ scan and rocking curve of the enlarged $Al_{0.8}Sc_{0.2}N$(0002) peak.

To study the chemical interaction between Pt and $Al_{0.8}Sc_{0.2}N$ film, *in-situ* XPS and UPS measurements were carried out on the Pt-deposited $Al_{0.8}Sc_{0.2}N$ film. Fig. 2 displays the Pt-thickness dependent XPS evolution of Sc 2p & N1s, Al 2p & Pt 4f, and Al 2s core-level spectra. In Fig. 2(a), the Sc 2p and N 1s regions of the pristine $Al_{0.8}Sc_{0.2}N$ surface have a similar binding energy range, where a single N 1s peak at 397.3 eV belongs to nitride. The Sc 2p region around 400–410 eV exhibits two significantly split spin-orbit sub-peaks, with the Sc $2p_{3/2}$ - $2p_{1/2}$ splitting of 4.5 eV. The main Sc $2p_{3/2}$ peaks can be further deconvoluted into Gaussian-Lorentzian two components, centered at 401.6 and 403.3 eV, which are assigned to Sc-N and Sc-O, respectively [32]. The Al 2p spectra of $Al_{0.8}Sc_{0.2}N$ in Fig. 2(b) shows two peaks originating from the Al-N (74.4 eV) and Al-O (75.4 eV) species, respectively [33-35]. After depositing 0.2 nm of Pt, a symmetric Pt $4f_{7/2}$ peak appears at a binding energy of 72.8 eV,

accompanied by a decrease in the intensity of the Al-N peak, as shown in Fig 2(b), (c) and Table S1. We suggest that this new peak originates from the Pt-N interaction between the Pt and N atoms in $Al_{1-x}Sc_xN$, because its binding energy is close to that of ionic Pt^{2+}-N bonds [36, 37]. Moreover, the reduction of the Al-N/Al-O ratio from 5.6 to 2.9 in the Al 2s region indicates that the generated Pt-N affects the bonding between Al and N atoms. It is known that the bond dissociation energy (BDE) of Sc-N (464 ± 84 kJ/mol) is larger than Al-N (≤ 368 ± 15 kJ/mol) [38], making it easier to substitute Al than Sc. Consequently, Pt tends to replace such Al atoms and form ionic Pt^{2+}–N bonds at the $Al_{0.8}Sc_{0.2}N$ interface. Upon 0.2 nm Pt deposition, all core-level peaks shift to lower binding energy by 0.2 eV, which can be explained by electron transfer from the $Al_{0.8}Sc_{0.2}N$ surface to Pt. However, there is no obvious peak shift or shape change in the O 1s region during the metal deposition process (Fig. S2(a)), indicating a weak interaction between platinum and oxygen. After 0.4 nm Pt deposition, the intensity of the Pt^{2+}-N signal in the Al 2p & Pt 4f regions does not increase simultaneously with thickness increase of Pt. Instead, a new distinct asymmetry Pt $4f_{7/2}$ peak appears at a much lower binding energy of 71.4 eV, which is attributed to the formation of metallic Pt. Additionally, the Al-N/Al-O ratio remains stable, suggesting that the chemical reaction between Pt and N in the $Al_{0.8}Sc_{0.2}N$ film only restricted in the interfacial regions. As the Pt thickness increases, the intensity of the metallic Pt peak increases dramatically, while the nitride and oxide peaks gradually attenuate in the XPS spectra. Meanwhile, all core levels of $Al_{0.8}Sc_{0.2}N$ continue to shift to lower binding energy with increasing Pt coverages, leading to an upward band-bending effect at the Pt/$Al_{0.8}Sc_{0.2}N$ interface.

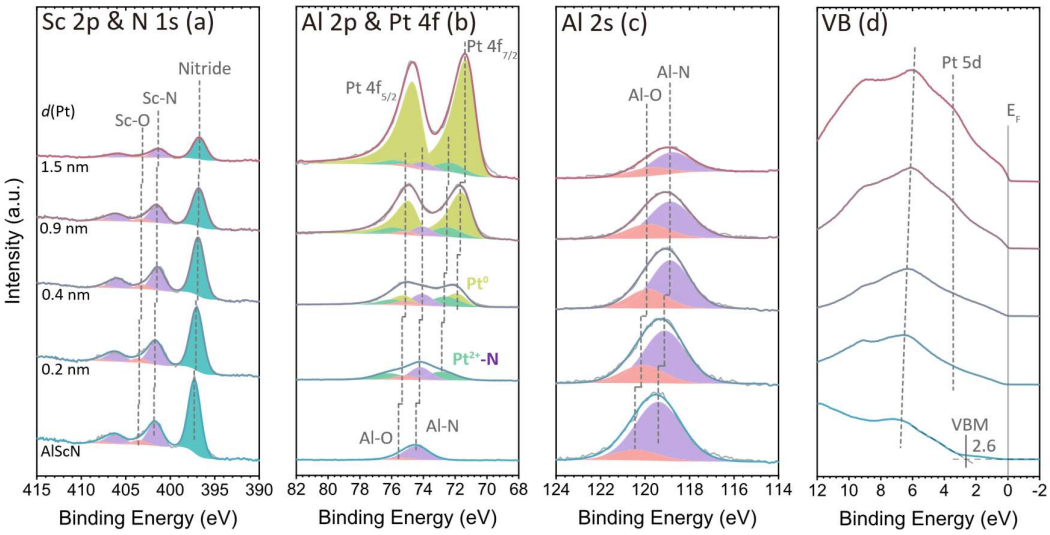

Fig. 2. Thickness dependent XPS spectra of (a) Sc 2p & N1s, (b) Al 2p & Pt 4f and (c) Al 2s for Pt/$Al_{0.8}Sc_{0.2}N$. UPS spectra of (d) valence band (VB) region with increasing thickness of Pt deposited on $Al_{0.8}Sc_{0.2}N$.

The change in the electronic structures for Pt deposition on $Al_{0.8}Sc_{0.2}N$ was further investigated by *in-situ* UPS characterization. As shown in Fig. 2(d), the valance band maximum (VBM) was determined by linear extrapolation of valance band onset minus the background around the Fermi level (E_F). As a result, the VBM of pristine $Al_{0.8}Sc_{0.2}N$ was found to be located at 2.6 eV below the E_F. The strong signal located between 4.3 to 8.5 eV was mainly formed by the state of the Al 3s, 3p and N 2p orbitals based on a previous theoretical study [39]. Upon Pt deposition, a new signal appears in the valence band at 3 eV, which was attributed to additional Pt 5d-derived electronic states [40, 41]. Furthermore, the intensity of the Pt 5d signal increased with increasing Pt coverage. The band-bending effects of Pt deposition on $Al_{0.8}Sc_{0.2}N$ were also observed in the UPS valence band spectra. Similar to the XPS core-level spectra, the characteristic valence band peak of pristine $Al_{0.8}Sc_{0.2}N$ at 6.6 eV shifted gradually to a lower binding energy by 0.6 eV after deposition of 1.5 nm of Pt. A clear Fermi edge appeared at 1.5 nm Pt thickness, indicating the formation of metallic Pt on $Al_{0.8}Sc_{0.2}N$. Electron transfer and formation of a Pt^{2+}-N bond at the Pt/$Al_{0.8}Sc_{0.2}N$ interface suggested that Pt atoms had incorporated into the aluminum scandium nitride lattice, which is an important Pt deposition process in $Al_{1-x}Sc_xN$ films.

The growth mechanism of Mo deposition on $Al_{0.8}Sc_{0.2}N$ was also investigated using *in-situ* XPS/UPS characterizations (Fig. 3). Upon depositing 0.2 nm of Mo, the binding energy of Sc 2p and N 1s regions in Fig. 3(a) overlapped with that of new Mo 3p signal, where the main Mo $3p_{3/2}$ peak is at 394.7 eV. Moreover, the asymmetric peak shape of the Mo $3d_{5/2}$ peak located at 228.6 eV indicated the presence of metallic Mo species on the $Al_{0.8}Sc_{0.2}N$ surface, as shown in Fig. 3(c). The peak shape of Mo 3d remained unchanged as the Mo coverage increased. Notably, the core-level XPS Mo $3d_{5/2}$ signal exhibited a shift in binding energy that decreased continuously due to the size-dependent effect caused by the increase in screening effects and the final-state energy variation for the metallic elements [42]. As depicted in Fig. 3(b) and Table S2, the Al-N/Al-O ratio in the Al 2p region stays unchanged during metal deposition. These results imply that deposited Mo does not bond with the substrate and appears as a pure metal on the $Al_{0.8}Sc_{0.2}N$ interface. With Mo deposition, the VB spectra in Fig. 3(d) shows a new signal at 1.6 eV, which originates from the Mo 4d states [43]. After 0.7 nm Mo deposition, a clear Fermi edge appears, corresponding to the formation of Metallic Mo on $Al_{0.8}Sc_{0.2}N$ in XPS results. Thus, the interaction mechanism for Mo on $Al_{0.8}Sc_{0.2}N$ is different from Pt-induced chemical reaction according to our *in-situ* XPS/UPS measurements. Interestingly, as the thickness of Mo increased from 0.2 to 1.4 nm, all the core-level peaks in Sc 2p and N 1s, as well as in the Al 2p regions and the main VB peaks, undergo a significant shift of 0.6 eV to the lower binding energy. This band-bending phenomenon indicates a similar electron transfer effect induced by both Pt and Mo on the $Al_{0.8}Sc_{0.2}N$ surface. Our findings shed light on the growth behavior of Mo on $Al_{0.8}Sc_{0.2}N$ and provide insights into the similarities and differences in the interaction mechanism of Pt and Mo on this substrate.

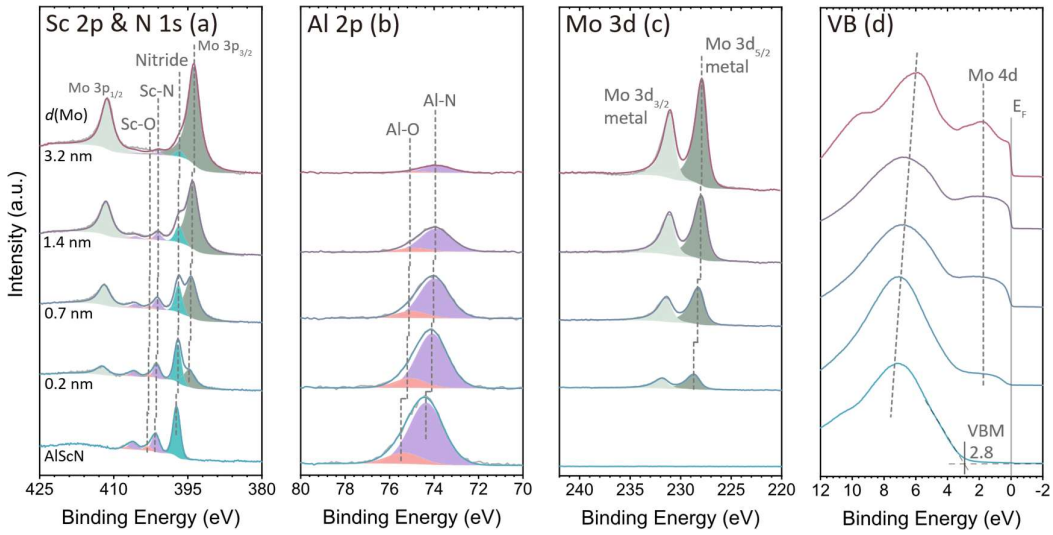

Fig. 3. XPS spectra of (a) Sc 2p & N 1s (with Mo 3p), (b) Al 2p, (c) Mo 3d, and UPS spectra of (d) valence band (VB) regions during Mo deposition on $Al_{0.8}Sc_{0.2}N$.

To assess the structural properties of the films, we examined the Pt/$Al_{0.8}Sc_{0.2}N$ and Mo/$Al_{0.8}Sc_{0.2}N$ interfaces using cross-sectional TEM. Fig. 4(a) displays a Pt film with a thickness of approximately 4.1 nm that was deposited onto a $Al_{0.8}Sc_{0.2}N$/Si(100) structure. The magnified high-resolution TEM image in Fig. 4(b) shows the interface between Pt and $Al_{0.8}Sc_{0.2}N$ with the minor disorder, with the direct deposition of $Al_{0.8}Sc_{0.2}N$ on Si substrate without any transitional amorphous layer. Although the crystal structure and morphology of the interface are not perfect, the orientation of $Al_{0.8}Sc_{0.2}N$ observed in the first few nanometers of Pt film growth remains roughly the original lattice structure. The average interlayer distance of 0.25 nm corresponds to the (0002) plane of the $Al_{0.8}Sc_{0.2}N$ thin film, while the Pt deposit shows an interlayer distance of 0.22 nm, corresponding to its (111) plane. Structural defects in complex multicomponent lattices at interface upon sputter deposition of metals or $Al_{1-x}Sc_xN$ has been reported previously [13, 24], but their reaction mechanism and surface layer chemical composition have been overlooked. In combination with the *in-situ* XPS/UPS measurements in this study, it was revealed that the interface between Pt and $Al_{0.8}Sc_{0.2}N$ is not smooth due to Pt diffusing into the $Al_{0.8}Sc_{0.2}N$ film and undergoing chemical reactions.

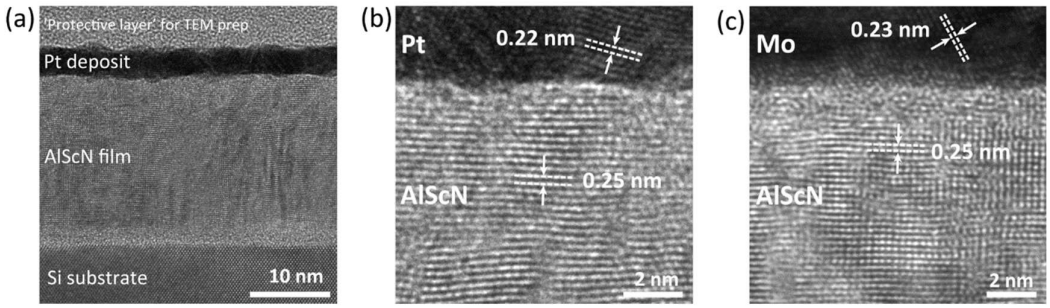

Fig. 4. (a) The cross-sectional TEM image of Pt deposited on the $Al_{0.8}Sc_{0.2}N$/Si substrate. High-resolution TEM images of (b) Pt/$Al_{0.8}Sc_{0.2}N$ and (c) Mo/$Al_{0.8}Sc_{0.2}N$ interfaces.

Fig. 4(c) presents a high-resolution cross-sectional TEM image of the interface between the 6.5 nm Mo deposit and $Al_{0.8}Sc_{0.2}N$ layers. The high-resolution TEM image shows the absence of an amorphous layer between the Mo and $Al_{0.8}Sc_{0.2}N$ interface. The average interplanar distance of 0.25 nm corresponds to the lattice plane (0002) spacing of the wurtzite crystalline phase in the pristine $Al_{0.8}Sc_{0.2}N$ film. Small crystals with an interlayer distance of around 0.23 nm were visible in the middle region of Mo layer. These results show that the deposition of Mo on $Al_{0.8}Sc_{0.2}N$ resulted in a homogeneous interface [44, 45].

Fig. 5 shows HAADF-STEM images of Pt/$Al_{0.8}Sc_{0.2}N$/Si and Mo/$Al_{0.8}Sc_{0.2}N$/Si structures, along with a line scan elemental profile plot of Pt/Mo, Al, Sc, N, O, and Si for the corresponding area, which were utilized to explore the compositional distribution at interfaces. As illustrated in Fig. 5(a), the Pt and $Al_{0.8}Sc_{0.2}N$ layers overlap at the interface, and the distribution of Pt shows a complex intermixing with $Al_{0.8}Sc_{0.2}N$. The initial 20 nm-thick $Al_{0.8}Sc_{0.2}N$ layer was reduced to approximately 18.3 nm due to Pt diffusion. Musavigharavi et al. [46] investigated the strain distribution between the $Al_{1-x}Sc_xN$ and Pt bottom electrode, revealing a higher defect density at the bottom close to the $Al_{1-x}Sc_xN$/Pt interface. In another study, it was reported that diffusion from the Pt bottom electrode to the AlN layer during the annealing process could lead to a loss in the resistive switching (RS) behavior and electrical short circuit of the crossbar array devices [47]. Local imperfections in metal layer intermixing and complex multicomponent lattices can significantly affect stability and crystal formation. Conversely, in the STEM-EDS line profile of the Mo/$Al_{0.8}Sc_{0.2}N$ interface demonstrated in Fig. 5(b), Mo and $Al_{0.8}Sc_{0.2}N$ layers

were clearly identified and Mo was not detected inside the $Al_{0.8}Sc_{0.2}N$ layer. No diffusion from the Mo top electrode into the $Al_{0.8}Sc_{0.2}N$ layer was observed during the deposition process, indicating a reliable homogeneous interface with no intermixing between the layers.

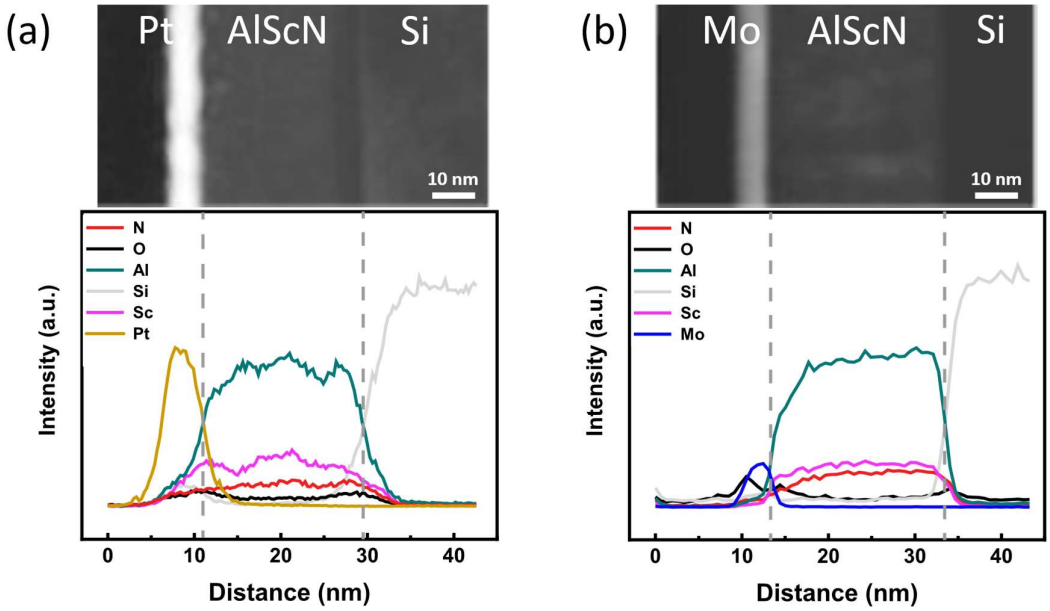

Fig. 5. The HAADF-STEM image and the EDS line scan element profile plot of the (a) Pt/$Al_{0.8}Sc_{0.2}N$/Si and (b) Mo/$Al_{0.8}Sc_{0.2}N$/Si heterostructures. Dashed line indicates the metal /$Al_{0.8}Sc_{0.2}N$ and $Al_{0.8}Sc_{0.2}N$/Si interfaces.

We carried out the additional characterization of the heterostructures using X-ray diffraction (XRD). Fig. S3(a) shows the assessment of the $Al_{0.8}Sc_{0.2}N$(0002) preferred orientation and crystal quality of films. The XRD rocking curves of the (0002) on pristine $Al_{0.8}Sc_{0.2}N$, Pt/$Al_{0.8}Sc_{0.2}N$, and Mo/$Al_{0.8}Sc_{0.2}N$ films are compared in Fig. S3(b), with full width at half maximum (FWHM) values of 0.58°, 0.67°, and 0.58°, respectively. Additionally, it becomes clear that the characteristic(0002) peak position of Pt/$Al_{0.8}Sc_{0.2}N$ film is shifted to a lower angle relative to pristine $Al_{0.8}Sc_{0.2}N$, likely due to a larger lattice constant results from the substitution of Al by Pt in crystal lattice [44]. Conversely, there was no significant shift in peak positions after Mo deposition, consistent with our XPS and TEM results, which showed that the deposition of Mo did not affect the crystal structure of $Al_{0.8}Sc_{0.2}N$. Nonetheless, it should be noted that internal stress effects introduced during the deposition process could also contribute to the observed peak shifts. Fig. S4 displays 2 μm × 2 μm morphological AFM maps of the

$Al_{0.8}Sc_{0.2}N$ surface after Pt and Mo deposition. As depicted in Fig. S4(a), a significant increase in RMS roughness at 2.30 nm and modification of the surface morphology occurred after Pt deposition. In particular, circular-shaped agglomerates appeared on the contact surface. This increase in roughness is related to the chemical reaction occurring in the Pt/$Al_{0.8}Sc_{0.2}N$ interface, as discussed earlier. On the other hand, the AFM scan of the as-deposited Mo/$Al_{0.8}Sc_{0.2}N$ sample in Fig. S4(b) shows a relatively smooth surface with an RMS roughness of 1.49 nm.

4 Conclusions

In conclusion, this study provides a comprehensive understanding of the electronic structures and chemical interactions at the interface between ultrathin Pt and Mo films and $Al_{1-x}Sc_xN$ by employing *in-situ* XPS and UPS studies. Strong chemical interaction and the formation of Pt^{2+}-N bonds between Pt and $Al_{0.8}Sc_{0.2}N$ substrate were observed, whereas Mo appears as a pure metal on the $Al_{0.8}Sc_{0.2}N$ surface. Furthermore, electron transfer-induced upward band-bending-like effects were observed on the $Al_{0.8}Sc_{0.2}N$ surface during both Pt and Mo deposition processes. We also examined the interface quality of Pt/$Al_{0.8}Sc_{0.2}N$ and Mo/$Al_{0.8}Sc_{0.2}N$ by employing complementary cross-sectional TEM and STEM–EDS line-scan. A complex intermixing layer near the Pt/$Al_{0.8}Sc_{0.2}N$ interface due to Pt diffusion was verified, while Mo/$Al_{0.8}Sc_{0.2}N$ shows a clear interface with no obvious interfacial defects, suggesting that Mo could be a promising top metal electrode for further research on $Al_{1-x}Sc_xN$-based devices. These findings provide fundamental insights into the growth mechanism and interfacial chemistry between metal electrodes and $Al_{1-x}Sc_xN$, which can contribute to the development of $Al_{1-x}Sc_xN$-based high-performance next-generation MEMS devices.

Supplementary material

XPS spectra of air-exposed and subsequently Ar^+ sputtering for pristine $Al_{0.8}Sc_{0.2}N$; O 1s XPS regions for $Al_{0.8}Sc_{0.2}N$ surfaces with increasing thickness of Pt and Mo; XRD and AFM characterizations of $Pt/Al_{0.8}Sc_{0.2}N$ and $Mo/Al_{0.8}Sc_{0.2}N$ thin films; Peak assignment of different components in XPS spectra and detailed peak fitting parameters.

Acknowledgment

The authors acknowledge the financial support from the Natural Science Foundation of China (62274118, U2032147), Singapore MOE Grant MOE-T2EP50220-0001, the Science and Engineering Research Council of A*STAR (Agency for Science, Technology and Research) Singapore under Grant No. A20G9b0135 and Singapore National Research Foundation Investigatorship Program under Grant No. NRF-NRFI08-2022-0009.

References

[1] Y.Q. Fu, J.K. Luo, N.T. Nguyen, A.J. Walton, A.J. Flewitt, X.T. Zu, Y. Li, G. McHale, A. Matthews, E. Iborra, H. Du, W.I. Milne, Advances in piezoelectric thin films for acoustic biosensors, acoustofluidics and lab-on-chip applications, Progress in Materials Science, 89 (2017) 31-91.

[2] M.A. Khan, M. Shatalov, H. Maruska, H. Wang, E. Kuokstis, III–nitride UV devices, Japanese journal of applied physics, 44 (2005) 7191.

[3] A. Danielraj, S. Deb, A. Mohanbabu, R.S. Kumar, The impact of a recessed Δ-shaped gate in a vertical CAVET AlGaN/GaN MIS-HEMT for high-power low-loss switching applications, Journal of Computational Electronics, 21 (2022) 169-180.

[4] R. Angamuthu, B. ChettiaGoundar Sengodan, M. Anandan, A. Varghese, B.S. Vakkalakula, LG 55 nm T-gate InGaN/GaN channel based high electron mobility transistors for stable transconductance operation, International Journal of RF and Microwave Computer-Aided Engineering, 32 (2022) e23308.

[5] A. Mohanbabu, N. Mohankumar, D.G. Raj, P. Sarkar, Investigation of enhancement mode HfO_2 insulated N-polarity GaN/InN/GaN/$In_{0.9}Al_{0.1}N$ heterostructure MISHEMT for high-frequency applications, Physica E: Low-dimensional Systems and Nanostructures, 92 (2017) 23-29.

[6] G. Chen, M. Rinaldi, Aluminum nitride combined overtone resonators for the 5G high frequency bands, Journal of Microelectromechanical Systems, 29 (2020) 148-159.

[7] Y. Liu, Y. Cai, Y. Zhang, A. Tovstopyat, S. Liu, C. Sun, Materials, design, and characteristics of bulk acoustic wave resonator: A review, Micromachines, 11 (2020) 630.

[8] C.C. Ruppel, Acoustic wave filter technology–a review, IEEE transactions on ultrasonics, ferroelectrics, and frequency control, 64 (2017) 1390-1400.

[9] S. Mertin, B. Heinz, O. Rattunde, G. Christmann, M.-A. Dubois, S. Nicolay, P. Muralt, Piezoelectric and structural properties of c-axis textured aluminium scandium nitride thin films up to high scandium content, Surface and Coatings Technology, 343 (2018) 2-6.

[10] M. Akiyama, K. Kano, A. Teshigahara, Influence of growth temperature and scandium concentration on piezoelectric response of scandium aluminum nitride alloy thin films, Applied Physics Letters, 95 (2009) 162107.

[11] M. Moreira, J. Bjurström, I. Katardjev, V. Yantchev, Aluminum scandium nitride thin-film bulk acoustic resonators for wide band applications, Vacuum, 86 (2011) 23-26.

[12] J.-c. Yang, X.-q. Meng, C.-t. Yang, Y. Zhang, Influence of sputtering power on

crystal quality and electrical properties of Sc-doped AlN film prepared by DC magnetron sputtering, Applied surface science, 287 (2013) 355-358.

[13] S. Fichtner, N. Wolff, F. Lofink, L. Kienle, B. Wagner, AlScN: A III-V semiconductor based ferroelectric, Journal of Applied Physics, 125 (2019) 114103.

[14] W. Wang, P.M. Mayrhofer, X. He, M. Gillinger, Z. Ye, X. Wang, A. Bittner, U. Schmid, J. Luo, High performance AlScN thin film based surface acoustic wave devices with large electromechanical coupling coefficient, Applied physics letters, 105 (2014) 133502.

[15] Z.A. Schaffer, G. Piazza, S. Mishin, Y. Oshmyansky, Super high frequency simple process flow cross-sectional Lamé mode resonators in 20% scandium-doped aluminum nitride, in: 2020 IEEE 33rd International Conference on Micro Electro Mechanical Systems (MEMS), IEEE, 2020, pp. 1281-1284.

[16] S. Shao, Z. Luo, T. Wu, High figure-of-merit Lamb wave resonators based on $Al_{0.7}Sc_{0.3}N$ thin film, IEEE Electron Device Letters, 42 (2021) 1378-1381.

[17] J. Wang, Y. Zheng, A. Ansari, Ferroelectric Aluminum Scandium Nitride Thin Film Bulk Acoustic Resonators with Polarization-Dependent Operating States, physica status solidi (RRL) – Rapid Research Letters, 15 (2021) 2100034.

[18] F. Cemin, D. Lundin, D. Cammilleri, T. Maroutian, P. Lecoeur, T. Minea, Low electrical resistivity in thin and ultrathin copper layers grown by high power impulse magnetron sputtering, Journal of Vacuum Science & Technology A: Vacuum, Surfaces, and Films, 34 (2016) 051506.

[19] P.P. Shinde, P. Tagade, S.P. Adiga, A. Konar, S. Pandian, K.S. Mayya, H.-J. Shin, Y. Cho, S. Park, Electrical resistivity of atomically smooth single-crystal Cu films, Physical Review B, 102 (2020) 165102.

[20] S. Fichtner, N. Wolff, G. Krishnamurthy, A. Petraru, S. Bohse, F. Lofink, S. Chemnitz, H. Kohlstedt, L. Kienle, B. Wagner, Identifying and overcoming the interface originating c-axis instability in highly Sc enhanced AlN for piezoelectric micro-electromechanical systems, Journal of Applied Physics, 122 (2017) 035301.

[21] M.A. Dubois, P. Muralt, Stress and piezoelectric properties of aluminum nitride thin films deposited onto metal electrodes by pulsed direct current reactive sputtering, Journal of Applied Physics, 89 (2001) 6389-6395.

[22] X. Liu, D. Wang, K.-H. Kim, K. Katti, J. Zheng, P. Musavigharavi, J. Miao, E.A. Stach, R.H. Olsson, III, D. Jariwala, Post-CMOS Compatible Aluminum Scandium Nitride/2D Channel Ferroelectric Field-Effect-Transistor Memory, Nano Letters, 21 (2021) 3753-3761.

[23] A. Das, M. Rath, D.R. Nair, M.S. Ramachandra Rao, A. DasGupta, Realization of preferential (100) oriented AlN thin films on Mo coated Si substrate using reactive RF

magnetron sputtering, Applied Surface Science, 550 (2021) 149308.

[24] D. Wang, J. Zheng, P. Musavigharavi, W. Zhu, A.C. Foucher, S.E. Trolier-McKinstry, E.A. Stach, R.H. Olsson, Ferroelectric switching in sub-20 nm aluminum scandium nitride thin films, IEEE Electron Device Letters, 41 (2020) 1774-1777.

[25] R. Nie, S. Shao, Z. Luo, X. Kang, T. Wu, Characterization of Ferroelectric $Al_{0.7}Sc_{0.3}N$ Thin Film on Pt and Mo Electrodes, Micromachines, 13 (2022) 1629.

[26] M. Li, H. Lin, K. Hu, Y. Zhu, Oxide overlayer formation on sputtered ScAlN film exposed to air, Applied Physics Letters, 121 (2022) 111602.

[27] Z. Ma, X. Lian, K. Yuan, S. Sun, C. Gu, J.L. Zhang, J. Lyu, J.-Q. Zhong, L. Liu, H. Li, W. Chen, Pressure-dependent band-bending in ZnO: A near-ambient-pressure X-ray photoelectron spectroscopy study, Journal of Energy Chemistry, 60 (2021) 25-31.

[28] L. Peize, L. Xu, G. Jian, D. Sisheng, D. Yishui, N. Yuxiang, C. Wei, *In-situ* near-ambient-pressure photoelectron spectroscopy investigations of high-work-function MoO_3 on 4H-SiC(0001), Surface Science, 729 (2023) 122234.

[29] F. Bartoli, J. Streque, J. Ghanbaja, P. Pigeat, P. Boulet, S. Hage-Ali, N. Naumenko, A. Redjaïmia, T. Aubert, O. Elmazria, Epitaxial Growth of $Sc_{0.09}Al_{0.91}N$ and $Sc_{0.18}Al_{0.82}N$ Thin Films on Sapphire Substrates by Magnetron Sputtering for Surface Acoustic Waves Applications, Sensors, 20 (2020) 4630.

[30] M. Park, Z. Hao, R. Dargis, A. Clark, A. Ansari, Epitaxial Aluminum Scandium Nitride Super High Frequency Acoustic Resonators, Journal of Microelectromechanical Systems, 29 (2020) 490-498.

[31] D. Wang, J. Zheng, Z. Tang, M. D'Agati, P.S. Gharavi, X. Liu, D. Jariwala, E.A. Stach, R.H. Olsson, V. Roebisch, Ferroelectric *c*-axis textured aluminum scandium nitride thin films of 100 nm thickness, in: 2020 Joint Conference of the IEEE International Frequency Control Symposium and International Symposium on Applications of Ferroelectrics (IFCS-ISAF), IEEE, 2020, pp. 1-4.

[32] M.C. Biesinger, L.W.M. Lau, A.R. Gerson, R.S.C. Smart, Resolving surface chemical states in XPS analysis of first row transition metals, oxides and hydroxides: Sc, Ti, V, Cu and Zn, Applied Surface Science, 257 (2010) 887-898.

[33] P. Motamedi, K. Cadien, XPS analysis of AlN thin films deposited by plasma enhanced atomic layer deposition, Applied Surface Science, 315 (2014) 104-109.

[34] F. Jose, R. Ramaseshan, S. Dash, S. Bera, A. Tyagi, B. Raj, Response of magnetron sputtered AlN films to controlled atmosphere annealing, Journal of Physics D: Applied Physics, 43 (2010) 075304.

[35] W. Wang, Y.Q. Fu, J. Chen, W. Xuan, J. Chen, X. Wang, P. Mayrhofer, P. Duan, A. Bittner, U. Schmid, AlScN thin film based surface acoustic wave devices with enhanced

microfluidic performance, Journal of Micromechanics and Microengineering, 26 (2016) 075006.

[36] G.M. Veith, A.R. Lupini, L. Baggetto, J.F. Browning, J.K. Keum, A. Villa, L. Prati, A.B. Papandrew, G.A. Goenaga, D.R. Mullins, S.E. Bullock, N.J. Dudney, Evidence for the Formation of Nitrogen-Rich Platinum and Palladium Nitride Nanoparticles, Chemistry of Materials, 25 (2013) 4936-4945.

[37] T. Li, J. Liu, Y. Song, F. Wang, Photochemical Solid-Phase Synthesis of Platinum Single Atoms on Nitrogen-Doped Carbon with High Loading as Bifunctional Catalysts for Hydrogen Evolution and Oxygen Reduction Reactions, ACS Catalysis, 8 (2018) 8450-8458.

[38] Y.-R. Luo, J.A. Kerr, Bond dissociation energies, CRC handbook of chemistry and physics, 89 (2012) 89.

[39] M. Zhu, L. Hua, F. Xiong, First principles study on the structural, electronic, and optical properties of Sc-doped AlN, Russian Journal of Physical Chemistry A, 88 (2014) 722-727.

[40] K. Schierbaum, S. Fischer, M. Torquemada, J. De Segovia, E. Roman, J. Martin-Gago, The interaction of Pt with TiO_2 (110) surfaces: a comparative XPS, UPS, ISS, and ESD study, Surface science, 345 (1996) 261-273.

[41] P. Blumentrit, M. Yoshitake, S. Nemšák, T. Kim, T. Nagata, XPS and UPS study on band alignment at Pt–Zn-terminated ZnO(0001) interface, Applied surface science, 258 (2011) 780-785.

[42] B. Johansson, N. Mårtensson, Core-level binding-energy shifts for the metallic elements, Physical Review B, 21 (1980) 4427.

[43] T. Schroeder, J. Zegenhagen, N. Magg, B. Immaraporn, H.-J. Freund, Formation of a faceted MoO_2 epilayer on Mo(112) studied by XPS, UPS and STM, Surface science, 552 (2004) 85-97.

[44] R. Dargis, A. Clark, A. Ansari, Z. Hao, M. Park, D. Kim, R. Yanka, R. Hammond, M. Debnath, R. Pelzel, Single-Crystal Multilayer Nitride, Metal, and Oxide Structures on Engineered Silicon for New-Generation Radio Frequency Filter Applications, physica status solidi (a), 217 (2020) 1900813.

[45] J. Kim, Low-temperature epitaxial growth of AlN thin films on a Mo electrode/sapphire substrate using reactive sputtering, Coatings, 11 (2021) 443.

[46] P. Musavigharavi, A.C. Meng, D. Wang, J. Zheng, A.C. Foucher, R.H. Olsson, III, E.A. Stach, Nanoscale Structural and Chemical Properties of Ferroelectric Aluminum Scandium Nitride Thin Films, The Journal of Physical Chemistry C, 125 (2021) 14394-14400.

[47] S.H. Won, S.H. Go, K.W. Lee, J.G. Lee, Resistive switching properties of Pt/TiO_2/n+-Si ReRAM for nonvolatile memory application, Electronic Materials Letters, 4 (2008) 29-33.